Removing Cadmium Impurities from Cation-Exchange-Derived $CuInSe_2/CuInS_2$ Nanorods for Enhanced Infrared Emission and Photodetection

Portniagin, Arsenii S.; Sergeev, Aleksandr A.; Sergeeva, Kseniia A.; Wang, Shixun; Li, Zhuo; Ning, Jiajia; Chan, Christopher C. S.; Kershaw, Stephen V.; Zhong, Xiaoyan; Wong, Kam Sing; Rogach, Andrey L.

Published in:
Advanced Functional Materials

Published: 22/08/2024

Document Version:
Final Published version, also known as Publisher's PDF, Publisher's Final version or Version of Record

Published version (DOI):
10.1002/adfm.202400942

Publication details:
Portniagin, A. S., Sergeev, A. A., Sergeeva, K. A., Wang, S., Li, Z., Ning, J., Chan, C. C. S., Kershaw, S. V., Zhong, X., Wong, K. S., & Rogach, A. L. (2024). Removing Cadmium Impurities from Cation-Exchange-Derived $CuInSe_2/CuInS_2$ Nanorods for Enhanced Infrared Emission and Photodetection. *Advanced Functional Materials*, *34*(34), Article 2400942. https://doi.org/10.1002/adfm.202400942

ADVANCED FUNCTIONAL MATERIALS
www.afm-journal.de

Removing Cadmium Impurities from Cation-Exchange-Derived $CuInSe_2/CuInS_2$ Nanorods for Enhanced Infrared Emission and Photodetection

Arsenii S. Portniagin, Aleksandr A. Sergeev, Kseniia A. Sergeeva, Shixun Wang, Zhuo Li, Jiajia Ning, Christopher C. S. Chan, Stephen V. Kershaw, Xiaoyan Zhong, Kam Sing Wong, and Andrey L. Rogach**

Metal chalcogenide nanocrystals with variable composition and shape can conveniently be produced using cation exchange synthesis; however, the presence of cation-containing ligands inherited from the starting material often results in contamination of the final product. To address this issue, a two-step ligand replacement strategy is developed to fabricate $CuInSe_2/CuInS_2$ nanorods from CdSe/CdS nanorods via removal of Cd-phosphonates from an intermediate $Cu_{2-x}Se/Cu_{2-x}S$ phase used in the cation exchange conversion. This synthetic approach furnishes $CuInSe_2/CuInS_2$ nanorods with cadmium content below 1 at.%, and high photoluminescence quantum yields reaching 40% in the near-infrared spectral range. Transient absorption studies reveal that the band alignment in the $CuInSe_2/CuInS_2$ heterostructure features a quasi-type II character, with an electron localized in the core and a hole wavefunction spread over the entire nanorod. The efficient passivation of the core and the reduced Cd content leads to excitonic emission with full width at half maximum down to 110 meV, superimposed with a broad emission band from copper-induced defects. Field-effect transistors based on cadmium-free $CuInSe_2/CuInS_2$ nanorods show two orders of magnitude lower noise current density compared with the cadmium-rich devices. The responsivity and specific detectivity of these devices reach 230 mA W^{-1} and 10^8 Jones, respectively, under near-infrared excitation at room temperature.

1. Introduction

On the nanoscale, cation exchange offers several advantages over direct synthetic means when either a metastable crystal structure or a non-spherical nanoparticle shape is desired.[1–4] A plethora of demonstrations of this approach were reported, such as the realization of peculiar material-shape/phase combinations which are inaccessible by conventional hot-injection routes,[5–14] precisely controlled shell thicknesses in the case of core/shell heterostructure synthesis,[15–18] and cation exchange driven phase transformations.[19] One of the material systems that can strongly benefit from the application of cation exchange synthesis is that of ternary chalcogenides, whose broad size distribution and compositional heterogeneity limit detailed studies of their optical properties.[20] More importantly, the defect-rich character of I-III-VI ternary chalcogenide nanocrystals usually leads to poor performance of devices fabricated thereof,[21–25] which oftentimes require

A. S. Portniagin, K. A. Sergeeva, S. Wang, Z. Li, S. V. Kershaw, X. Zhong, A. L. Rogach
Department of Materials Science and Engineering
City University of Hong Kong
83 Tat Chee Avenue, Kowloon Tong, Hong Kong SAR 999077, China
E-mail: andrey.rogach@cityu.edu.hk

A. A. Sergeev, C. C. S. Chan, K. S. Wong
Department of Physics
Hong Kong University of Science and Technology
Hong Kong SAR 999077, China
E-mail: phkswong@ust.hk

Z. Li, X. Zhong
City University of Hong Kong
Matter Science Research Institute (Futian, Shenzhen)
Shenzhen 518048, China

Z. Li, X. Zhong
Chengdu Research Institute
City University of Hong Kong
Chengdu 610200, China

The ORCID identification number(s) for the author(s) of this article can be found under https://doi.org/10.1002/adfm.202400942

DOI: 10.1002/adfm.202400942

high processing temperatures to anneal defects,[26–28] resulting in losing the benefits of solution processing on an arbitrary substrate. Cation exchange procedures, producing defect-rich nanocrystals at the dawn of the quantum dot era, have recently evolved into a versatile method that allows chemists to synthesize high-quality nanomaterials with outstanding performance in devices.[10,29] The latest synthesis strategies relied on ligand-assisted cation exchange and allowed for more balanced cation inflow and outflow avoiding Kirkendall-related defects and cavities,[30] with the employed ligands both slowing down the cation exchange and providing improved crystallinity and colloidal stability of the resulting nanocrystals.[31] While the effect of ligands added during cation exchange has become a major focus of studies recently,[32] the influence of the starting material's surfactant "fur coat" has often been overlooked. Even though purification of the starting materials excluded ligands from the previous synthetic step, the remaining portion of surfactants still may lead to significant contamination of the final product. Particularly, while the X- and L-type ligands, which are usually acid anions and neutral electron donors,[33] do not pose any potential threats as impurities, Z-type ligands, which are metal cation-based electron acceptors,[34,35] may become involved in the later stages of cation exchange. So far, many kinds of anisotropic nanocrystals have been prepared using cadmium chalcogenides followed by a cadmium-to-copper exchange step,[7,8,36,37] but the problem of (obviously, undesirable) Cd contamination was not resolved yet. Moreover, the metal-to-copper exchange step severely affects the surface structure and affinity toward phosphonic acids, thus rendering an important class of $Cu_{2-x}X$ (X = S, Se, or Te) nanocrystals insufficiently well stabilized by the ligands inherited from the previous step.[38] All these factors together significantly hinder the wider applicability of the cation exchange approaches toward high-quality nanocrystals in general, and anisotropic I-III-VI chalcogenides in particular.

Cation-exchange-driven contamination of ternary chalcogenides also complicates analysis of their optical properties, as the emission mechanism of, i.e., CuIn-chalcogenides is rather complex, involving an interplay between band-to-band and defect-assisted recombination, such as donor-acceptor pair recombination, defect level – valence band (VB) recombination, and conduction band (CB) – defect level recombination.[39–43] Generally, the recombination processes involving copper defects have been described as the recombination of a delocalized CB electron with a hole localized on the Cu defect. Klimov et al.[39,44,45] discussed the activation of the Cu^{1+} ion by photoexcitation, wherein an electron from the $3d^{10}$ configuration is excited to the CB, resulting in Cu^{2+} formation (a copper ion in a $3d^9$ configuration). In the case of copper vacancies, the copper ion is initially in a 2+ oxidation state and it is inherently optically active due to a hole-like vacancy.[39] Houtepen et al.[42] suggested that Cu^{2+} constitutes a "dark" state involved in efficient trap-assisted Auger recombination between the CB electron and a Cu^{2+} defect. However, such recombination is only possible in the presence of a photogenerated hole in the VB, which is then excited into a deeper energy level. This picture in fact correlates with that in Klimov's studies, where the possibility of radiative recombination between the CB electron and a Cu^{2+} site was only deemed to occur when a photogenerated hole was removed from the VB via trapping.[39] The high mobility of copper ions and the existence of Cu-In stoichiometry-dependent defects suppress the pure excitonic recombination, resulting in the consensus in the community that the main recombination pathway in those materials is defect-assisted. However, to verify the defect-assisted recombination, one has to exclude masking by the influence of size and compositional heterogeneity of the CuIn-based chalcogenides on the optical spectra, which can be achieved by means of cation exchange with the amount of cation impurities left over from the starting material to the final product being reduced to the absolute minimum.

In this study, we examined the effects of ligands on the metal-to-copper exchange step during the processing of CdSe/CdS nanorods (NRs) in a form of prototypical "dot-in-rod" structure,[46,47] subjected to the cation exchange conversion into $CuInSe_2/CuInS_2$ nanorods (we will denote them as CISe/CIS, later on). Our choice of these NRs was determined by their significant application potential in the field of bioimaging, photodetection, and photovoltaics,[48] owing to the better charge transport characteristics of NRs[37] and near-infrared (NIR) polarized emission with a large apparent Stokes shift. At the same time, due to the feasibility of the use of copper(I) complexes as thermodynamically favored reagents for a variety of metal chalcogenides cation exchange reactions,[3] the results obtained in this study can be easily generalized toward many other nanomaterials. We found out that Cd remains in the ligand shell sphere of intermediate $Cu_{2-x}Se/Cu_{2-x}S$ NRs in the form of phosphonates, and can enter the crystalline lattice of CISe/CIS NRs during the next, Cu-to-In cation exchange step, therefore contaminating the final product. We show that the X- and Z-type ligand exchange assisted by octylamine/trioctylphosphine oxide (TOPO) mixture enables the removal of cadmium phosphonates, reducing the Cd content by one order of magnitude as compared to the standard synthesis procedure. A somewhat diminished colloidal stability of the $Cu_{2-x}Se/Cu_{2-x}S$ NRs after ligand exchange was improved by the addition of TOPO alongside octylamine, while anion passivation was accomplished by the addition of In-phosphonates, thus compensating the loss of the Cd-containing Z-type ligands removed during the previous step. The resulting CISe/CIS NRs showed high photoluminescence (PL) quantum yield (QY) reaching 40%, which renders them the brightest anisotropic heavy-metal free near-infrared (NIR) luminophores reported in the literature, to the best of our knowledge. Transient absorption and time-resolved PL measurements elucidated a quasi-type II character of band alignment in the CISe/CIS NRs and provided useful insights on the effect of the Cd content on their optical properties. Furthermore, the electrical performance of CISe/CIS NRs has been evaluated in their field-effect transistor (FET)-based devices. The results revealed that the developed two-step ligand exchange facilitates effective surface defect passivation and significantly enhances charge carrier mobility. As a result, FET devices exhibited a responsivity of up to 230 mA W^{-1} under NIR illumination, and the noise current density of the heavy-metal-free

J. Ning
Key Laboratory of Physics and Technology for Advanced Batteries
Ministry of Education
College of Physics
Jilin University
Changchun 130012, China

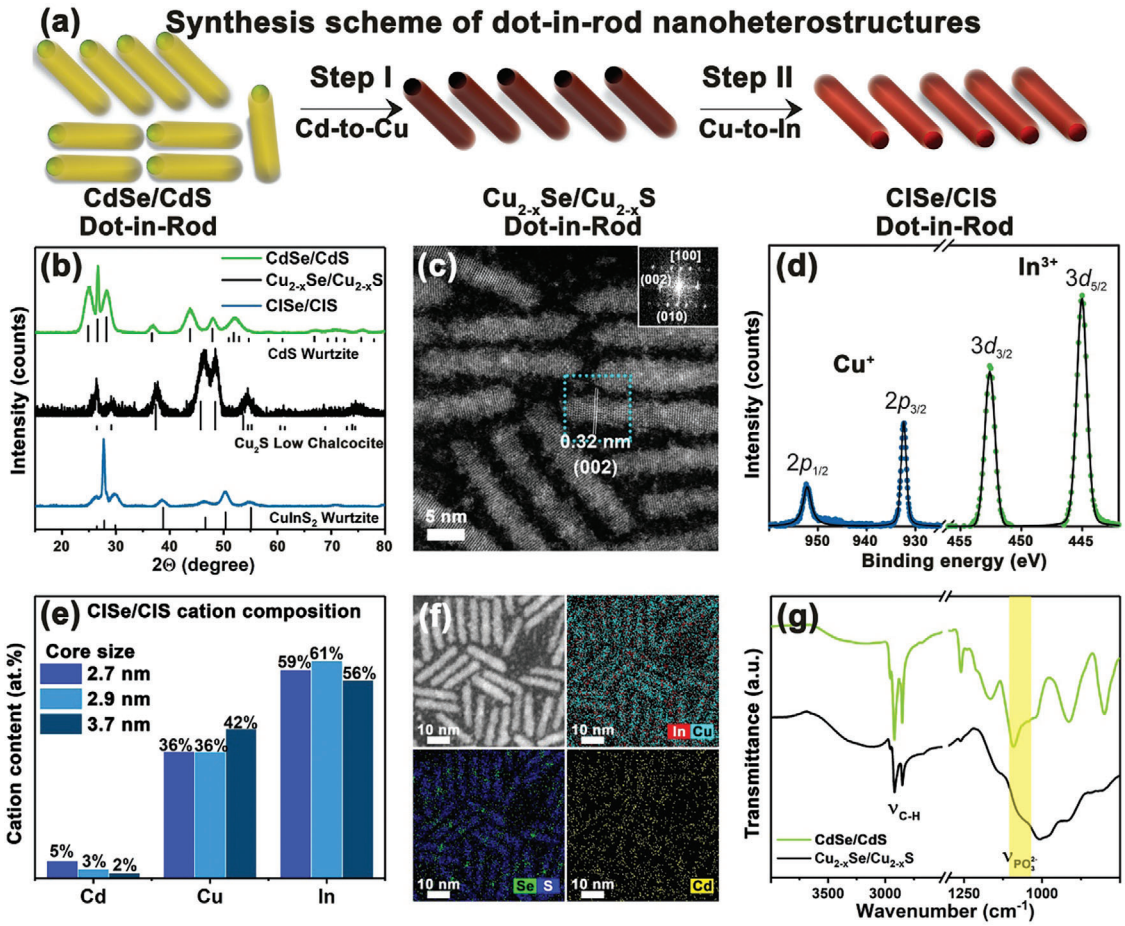

Figure 1. a) Two-step cation exchange synthesis scheme of CISe/CIS NRs starting from dot-in-rod CdSe/CdS NRs, with the formation of $Cu_{2-x}Se/Cu_{2-x}S$ NRs during the intermediate stage. b) XRD patterns of the 2.9 nm CdSe/CdS and CISe/CIS NRs. c) High-resolution HAADF-STEM image of the 2.9 nm CISe/CIS NRs. The blue-dotted rectangle indicates the area for which the FFT pattern is provided in the inset. d) XPS spectra of Cu2*p* and In3*d* bound states of CISe/CIS NRs. e) ICP-AES elemental composition of the CISe/CIS NRs of various core sizes. f) STEM images of 2.9 nm CISe/CIS NRs and EDX elemental mappings for {In + Cu}, {Se + S}, and Cd elements, presented using different color codes. g) FTIR spectra of Cd-based NRs and Cu-based NRs derived thereof. The yellow rectangle highlights the location of absorption bands related to the phosphonate anion stretching.

FETs was two orders of magnitude lower compared to the more significant residual Cd-containing ones.

2. Results and Discussion

2.1. Cation Exchange Synthesis of CISe/CIS NRs, Their Crystal Structure, and Composition

Cation exchange synthesis of CISe/CIS NRs starting from CdSe/CdS NRs comprised two steps, illustrated in **Figure 1a**. The first step was the Cd-to-Cu exchange using a methanol solution of copper(I) acetonitrile complex, followed by partial Cu-to-In cation exchange as the second step. As compared to the originally reported method of CISe/CIS NR synthesis by sequential cation exchange utilizing In(III) chloride-trioctylphosphine ($InCl_3$-TOP) complex,[8] In(III) acetate-trioctylphosphine ($In(OAc)_3$-TOP) has been used here as the indium(III) precursor, and dodecanethiol (DDT) – as a surfactant. The resulting CISe/CIS NRs had better colloidal stability than in the original report[8] and were less prone to aggregation as evidenced by transmission electron microscopy (TEM) images (Figure S1a,b, Supporting Information).

To study the influence of the CISe core size on the properties of the dot-in-rod CISe/CIS heterostructure, we used CdSe seeds of 2.7, 2.9, and 3.7 nm in diameter (Figure S2, Supporting Information). The corresponding NRs will be referred to "Y nm CdSe/CdS NRs" and "Y nm CISe/CIS NRs" derived thereof, where Y is the CdSe seed size. X-ray diffraction (XRD) patterns show that both Cd and Cu-In-based NRs adopt a wurtzite structure, confirming retention of this hexagonal phase after cation exchange (Figure 1b). Intermediate $Cu_{2-x}Se/Cu_{2-x}S$ NRs have low crystallinity due to a large number of defects caused by rapid Cd-to-Cu cation exchange events. The narrowest XRD peak at 27.66° 2θ (0. 32 nm d-spacing), associated with the (002) reflection, corresponds to the most developed crystal plane, which is further confirmed by an interplane spacing of 0.32 nm observed along the long axis of the NRs found by high-resolution TEM (HRTEM) (Figure 1c). The obtained CISe/CIS NRs were highly crystalline as supported by the distinct fringes on the Fast Fourier Transform (FFT) pattern (Figure 1c, inset). The proposed multistep synthetic

approach did not affect the NRs' size distribution significantly (Figure S3, Supporting Information), but the average CISe/CIS NR length systematically contracted in comparison to the starting Cd-based NRs due to the smaller lattice constants of $CuInS_2$ as compared to CdS.[49]

Since the cation exchange synthesis scheme (Figure 1a) implies managing several cationic species constituting the final NRs (Cd, Cu, In), the chemical composition of the obtained CISe/CIS NRs has then been studied in detail. Contrary to some of the known counterparts,[26] copper ions in CISe/CIS NRs are found to exist in the 1+ oxidation state. High-resolution core-level X-ray photoemission spectra (XPS) of Cu2*p* and In3*d*, which are shown in Figure 1d, display spin-orbit doublets with binding energy maxima at 932.4 and 952.4 eV (Cu^+) and 445 and 452.6 eV (In^{3+}), respectively. In turn, the positions of the Se3*d* and S2*p* peaks are associated with chalcogen–metal bonding (Figure S4, Supporting Information). Notably, no sub-peaks assigned to metal-oxygen bonds were observed. Using inductively coupled plasma atomic emission spectrometry (ICP-AES) we found the In:Cu cation ratio to be ≈1.7:1 regardless of the starting core size (Figure 1e). Previously, partial Cu-to-In cation exchange was considered to be thermodynamically self-limiting, due to the minimal mismatch between the anion sublattices of low-chalcocite Cu_2S and wurtzite $CuInS_2$ phases.[31] However, here we doubled the amount of In(III) acetate introduced into the reaction, which resulted in the In-rich composition of the final CISe/CIS NRs (Figure 1e).

Notably, a rather high Cd content in the resulting CISe/CIS NRs was determined by ICP-AES, ranging from 1.5 to 5.0 at.% depending on the core size (Figure 1e). It was reported previously that Cd was observed in the intermediate Cu chalcogenide NRs (see Figure 1a), but it apparently did not appear in the final CISe/CIS NRs.[8] We found that the extensive washing of $Cu_{2-x}Se/Cu_{2-x}S$ NRs had practically no effect on the Cd versus Cu content (Figure S5, Supporting Information), thus excluding adventitious Cd contamination by its surface adsorption after cation exchange. Furthermore, given the much lower solubility constant of Cu chalcogenides than that of Cd chalcogenides (10^{-48} vs 10^{-27}),[3] it is highly unlikely for Cd cations to be retained within the lattice at amounts of several atomic percent.

There is also a question about the exact distribution of the constituent elements in the final CISe/CIS NRs, i.e., if there is any difference in distribution between the core and the shell. Elemental mapping conducted by means of scanning TEM (STEM) energy dispersive X-ray spectroscopy (EDS) showed that the Cd distribution within the final CISe/CIS NRs was uniform, which was also the case for Cu and In elements, while Se (more in the core) and S (more in the shell) distributions clearly followed the intended core/shell architecture retained after the two exchange steps (Figure 1f(i–iv)).

Surface ligands are another form of possible Cd-bearing species. The surface of colloidal nanocrystals is generally known to be covered by L-type (neutral donors), X-type (negatively charged, acid anions), and Z-type (positively charged, ammonia, and metal cations) ligands.[50] While L-type ligands can be easily displaced and do not need a counterion, X- and Z-type ligands coexist with countercharged cations and anions, respectively, which is also the reason for the commonly encountered cation-rich surface of metal chalcogenide nanocrystals.[51] Synthesis of CdSe/CdS NRs usually involves Cd-phosphonates as a cation precursor, and thus these NRs will have X- and Z-type ligands in the final material. After Step I illustrated in Figure 1a, $Cu_{2-x}Se/Cu_{2-x}S$ NRs retained colloidal stability due to the phosphonate-containing ligands. Indeed, Fourier-transform infrared (FTIR) spectra shown in Figure 1g confirm the presence of alkyl phosphonate anions at the surface of $Cu_{2-x}Se/Cu_{2-x}S$ NRs, with stretching bands located at ≈1090 cm^{-1}.[52] The ^{31}P NMR spectrum further confirms the presence of bound phosphonates by a broadened peak centered at a shift of 33 ppm (Figure S6, Supporting Information), which corresponds well to previously reported values for phosphonate-capped Cd chalcogenides.[53] Such retaining of Cd source material in the phosphonate form at the surface of Cu-based NRs allows these cations to participate in Step II of the cation exchange (see Figure 1a). To confirm the hypothesis of the "ligand shell origin" of the Cd contamination in the final CISe/CIS NRs, we added oleate and phosphonate anions into the reaction mixture during Step I, which indeed led to increased Cd content in the final CISe/CIS NRs (Figure S7, Supporting Information). These free oleate and phosphonate anions can bind to Cd^{2+} cations, which are released during exchange and are harder Lewis acids as compared to Cu(I); they can partially be retained at the surface, and participate in the cation exchange at Step II (see Figure 1a). Addition of oleylamine as a neutral L-type ligand in Step I of the cation exchange was also found to increase the Cd content in the final CISe/CIS NRs up to 14–26 at.% depending on the core size (Figures S8 and S9, Supporting Information). At the same time, the presence of amines during the exchange in the toluene-methanol mixture keeps the morphology and size distribution of the NRs unchanged (Figure S10, Supporting Information).

Thus, it appears that Cd-phosphonates, serving as ligands during the Cd-based NR synthesis, are responsible for the Cd presence in the final NRs. Cadmium can enter the CISe/CIS lattice during Step II of the cation exchange, as it is conducted at elevated temperature under long exposure to TOP. Moreover, the addition of different ligands, either charged anions of common long-chain carboxylic/phosphonic acids or neutral amine ligands, tunes the Cd content through compositional alloying.

2.2. Octylamine-Assisted Removal of Cadmium Phosphonates and the Effect of the Remaining Cd Content on the Exciton Recombination in CISe/CIS Nanorods

As Cd-phosphonates were found to be the main source of the Cd contamination in the final CISe/CIS NRs, we conducted ligand exchange with octylamine, because primary amines are known to be very efficient X- and Z-type ligand displacement agents.[35] The removal of Cd was confirmed by ICP-AES (**Figure 2a**), clearly evidencing a more than 90% removal efficiency. Such high removal efficiency is in good agreement with the reported data on Z-type ligand displacement potency by amines, which were also claimed to exhibit over 90% removal of cadmium alkanoates previously.[35] This is corroborated by the completely suppressed absorption bands of phosphonates in the FTIR spectrum at 1090 cm^{-1} after ligand exchange with octylamine (OctAm), as shown in Figure 2b. However, the $Cu_{2-x}Se/Cu_{2-x}S$ NRs partially lost their colloidal stability after ligand exchange with OctAm,

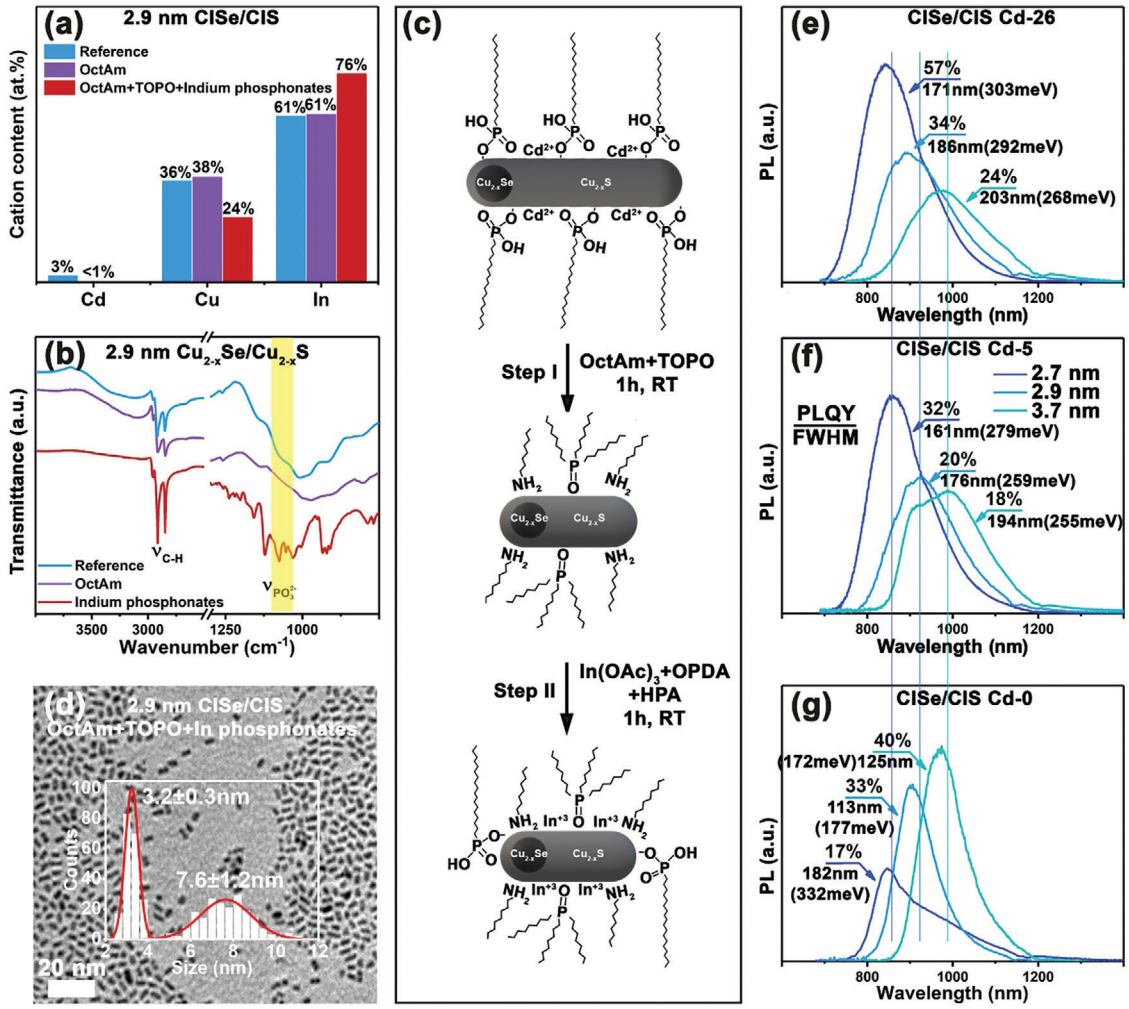

Figure 2. a) Cation composition of 2.9 nm CISe/CIS NRs determined by ICP-AES, depending on the ligand exchange conditions. b) FTIR spectra of $Cu_{2-x}Se/Cu_{2-x}S$ NRs after ligand exchange with octylamine and In-phosphonates. The yellow rectangle highlights absorption bands related to the phosphonate anion stretching modes. c) Two-step ligand replacement scheme: Step I involves the removal of Cd-phosphonates by using octylamine and TOPO, while in Step II In-phosphonates are added for colloidal stabilization via the passivation of anionic sites. d) TEM image of the 2.9 nm CISe/CIS NRs, with 3.2 nm diameter and 7.6 nm length. e–g) PL spectra of CISe/CIS NRs with varying Cd content, indicated in the brackets. Numbers on the graphs provide corresponding PL QY values.

and the CISe/CIS NRs derived thereof were rather inferior in terms of optical properties as compared to the samples produced under standard conditions. Given that the amine-capped nanocrystals are rather unstable at amine concentrations below 0.1 M,[54] any purification step after ligand exchange with OctAm can easily cause the $Cu_{2-x}Se/Cu_{2-x}S$ NRs to aggregate, which in turn yields unstable colloidal dispersions of CISe/CIS NRs with inferior PL.

To improve the colloidal stability of the intermediate $Cu_{2-x}Se/Cu_{2-x}S$ NRs, we used TOPO as a co-surfactant during the ligand exchange. TOPO is known to favor the formation of hexagonally structured Cu-based chalcogenides, such as Cu_2S,[55,56] Cu_2Se,[57] and Cu_2Te,[58] which implies that it possesses a high affinity toward the surface of the Cu chalcogenide nanocrystals with hexagonal atomic arrangements. Additional stabilization with TOPO as a co-surfactant indeed improved the colloidal stability of the Cu-based NRs and the CISe/CIS NRs derived thereof. Moreover, a combined TOPO and OctAm ligand exchange procedure resulted in an improvement of the PL QY of the resulting NRs from <1% up to 4%. However, such values still lag far behind the original untreated ones, with PL QYs of ≈20%. This may be a consequence of the removal of the mostly Z-type Cd-containing ligands, which are used to passivate the anionic sites of the Cu-based NR's surface, while no alternative stabilizing agents were provided to account for such a loss. To address this issue, we conducted an additional ligand treatment step by introducing In-phosphonates to the toluene solution of $Cu_{2-x}Se/Cu_{2-x}S$ NRs as a replacement for the displaced Cd-phosphonates (Figure 2c). Strong absorption bands in the FTIR spectrum at 1090 cm^{-1} (Figure 2b) indicate the replenishment of the phosphonate capping after this additional ligand exchange. We also noticed that apart from colloidal stabilization, the presence of phosphonic acids at the surface of the NRs reduced the reactivity of In-containing precursors during

the cation exchange, making the cation's inter-diffusion slower and better balanced. Previously, inorganic[59,60] and long-chain organic salts[61] were shown to improve both colloidal stability and emission of the as-synthesized nanocrystals. It should be noted that CISe/CIS NRs contained no phosphonates according to FTIR spectra (Figure S11, Supporting Information), as a large molar excess of DDT replaced phosphonates during the Cu-to-In cation exchange step.

The final CISe/CIS NRs were characterized by a somewhat etched (reduced dimension) particle morphology (Figure 2d), as a result of the simultaneous action of the amine and TOPO. Amines are known to coordinate strongly with Cu(II) species,[62] and owing to the non-stoichiometric character of Cu chalcogenides and the high specific surface area of the NRs, the latter can become partially etched at the surface by these ligands. TEM images of $Cu_{2-x}Se/Cu_{2-x}S$ NRs taken before and after treatment with the OctAm-TOPO mixture further corroborated that the etching took place during this ligand-exchange step (Figure S12, Supporting Information). We also observed surface etching for the 2.7 and 3.7 nm CISe/CIS NRs (Figure S13, Supporting Information), whose degree was proportional to the specific surface area of NRs. Specific surface area decreases in the order 2.7 nm > 2.9 nm > 3.7 nm CISe/CIS, and so does the degree of their etching, resulting in the reduction of the NR's geometrical dimensions (Figure S13 vs Figure S3, Supporting Information). Still, the Cd content in all three NR systems was suppressed toward <1 at.% (Figures S14 and S15, Supporting Information), confirming the successful implementation of the proposed two-step ligand exchange procedure (Figure 2c).

The compositional tunability achieved with the introduced ligand exchange procedure allowed us to examine the effects of the Cd amount in the CISe/CIS NR on their optical properties. Absorption spectra of the CISe/CIS NRs show rather sharp absorption edges corresponding to the CIS shell (Figure S16, Supporting Information), unlike the comparatively featureless absorption spectrum of CISe/CIS core/shell quantum dots[63] and NRs[8] studied previously. This underscores the main asset of cation exchange synthetic strategies, namely establishing and preserving the narrow size distribution of the starting materials, rather than dealing with a broader distribution in the direct synthesis. While the high Cd content (up to 26 at.%, hereinafter referred as Cd-26) samples prepared by the addition of oleylamine during the Cd-to-Cu cation exchange step practically didn't alter the absorption spectra, etching in the case of low Cd (<1 at.%, sample Cd-0) NRs led to somewhat deteriorated diameter/length distributions (Figure S13a, Supporting Information), and resulted in a blue-shift of the absorption edge for 2.7 and 2.9 nm CISe/CIS (Figure S16, Supporting Information). These samples also exhibited featureless band edges of their absorption spectra compared to samples with unaltered rod-like morphology. The shape of their emission profiles, on the other hand, was altered depending on the Cd content (Figure 2e–g). Blueshifts of PL bands in the cases of higher Cd content were frequently reported for ternary nanocrystals, particularly when alloying occurred.[49,64,65] The PL band blue-shifts in the Cd-0 series due to the increased quantum confinement because of contracted NR size or the changed band alignment in the CISe/CIS heterostructure, altering recombination pathways in Cd-0 NRs as compared to samples with medium Cd content (up to 5 at.%, sample Cd-5). While higher Cd content generally results in the improvement of PL emission regardless of the core size, in the case of Cd-0 series 2.7 nm CISe/CIS NRs, which were etched the most, demonstrated the reduced PL efficiency, contrary to their larger counterparts (Figure 2e–g).

2.3. Charge Carrier Dynamics in CISe/CIS Nanorods

To further investigate the recombination pathways and the effects of chemical composition on the optical properties of CISe/CIS NRs, we conducted transient absorption (TA) studies. TA spectra revealed a broad positive $\Delta T/T$ band matching the minima in the second derivative of the linear absorption as shown in **Figure 3a**. The minimum of the second derivative centered at ≈700 nm, corresponds to the position of the shell CB, while the other minimum, centered at ≈840 nm, can be attributed to the core's bandgap in CISe/CIS core-shell NRs. This is supported by the consistent changes in the spectral position of these bands with the size of the NRs (Figure S17, Supporting Information). Therefore, these bands can be attributed to the ground-state bleach (GSB) for the shell and the core states, respectively. At the higher-energy side of the TA spectra, we observed a series of relatively weak positive peaks superimposed on the broad photoinduced absorption (PA) band. The absorption dips centered at 515 and 605 nm closely matched the corresponding minima in the second derivative, and thus could be attributed to the high-energy transitions occurring in the CIS shell. We notice that the shell in CISe/CIS NRs has a much larger absorption cross-section than the core due to its larger volume, and hence the optical response from the shell states is much stronger. The overlapping PA band is attributed to refractive index changes and bandgap renormalization appearing after photoexcitation, leading to high-energy negative features.[66]

By probing the shell and the core states at the peak wavelengths, we obtained the dynamics of photo-excitation transfer as a difference in the rise-time for the CIS shell and CISe core GSBs (top panel of Figure 3c). Under the shell-state excitation, the CISe core's GSB rise time for larger-sized NRs remained almost the same, ≈5 ps (Figure S18, Supporting Information). However, for the smallest NRs, it increased significantly to 11 ps, likely due to the higher trap density on the core/shell interface. Once built up, the core's GSBs decayed slowly, with a decay half-time that extended beyond the delay time range of our TA setup (1 ns).

The observed energy transfer from the shell to the core suggests that the core's CB is positioned lower than the shell's, leading to the localization of electrons within the core of the CISe/CIS NRs. Furthermore, when the core was resonantly excited in the 780–930 nm range (depending on the core's size, for 2.9 nm-sized NRs the excitation wavelength is 830 nm, as shown in Figure 3b), we observed a rapid instrumental response-limited rise of the shell's GSB at the same rate as the core's GSB (Figure 3c, bottom panel). This phenomenon is likely due to photoinduced hole transfer from the core to the shell, indicating that the shell's VB is at the same or a slightly higher level than the core's in CISe/CIS NRs. This behavior was consistent across varying core sizes and Cd content in the studied CISe/CIS

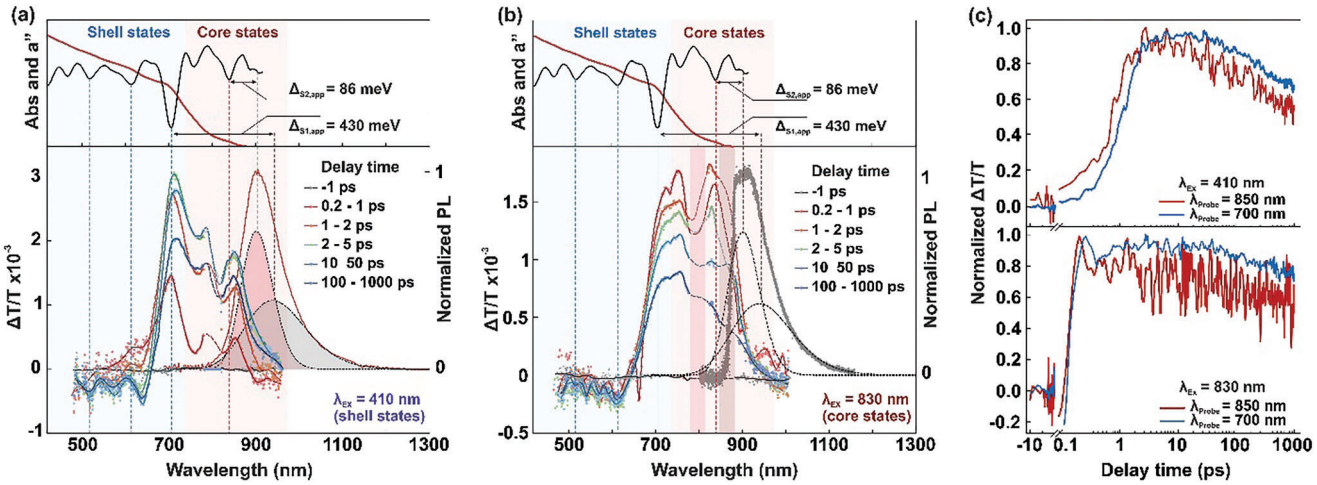

Figure 3. a,b) TA spectra measured at different delay times for 2.9 nm Cd-0 CISe/CIS NRs under excitation with photon energies above the CIS shell's bandgap (a) and resonantly into the core states (b). The top panels show the linear absorption spectrum and its second derivative (a''). The dashed vertical lines are to guide the eye to the relative positions of a'' minima and TA bands. c) Kinetics of the CIS shell's and the CISe core's GSB probed with excitation above the shell's bandgap (top) and resonant excitation into the core's bandgap (bottom).

NRs (Figure S19, Supporting Information), indicating a quasi-type II band alignment with an electron confined in the core and a hole distributed throughout the heterostructure (both in the core and the shell) in all samples. Moreover, we observed a similar transfer in the parent CdSe/CdS NRs, confirming the maintenance of the core/shell heterostructure with quasi-type II band alignment after cation exchange (Note S1, Supporting Information).

2.4. Emission Mechanism in CISe/CIS Nanorods

We noticed the trapping of VB holes from the TA kinetics, as evidenced by the rapid quenching of the GSB within 1 ps after excitation (Figure 3c), which is consistent with previous research findings.[67] Moreover, in our CISe/CIS NRs, the hole extraction from the core is enhanced by a quasi-type II band alignment, resulting in two competitive emission pathways appear as evident from the two-band PL spectrum (Figure 2e–g) and different decay times of short- and long-wavelength shoulders of the PL spectrum (**Figure 4a**). We extracted the relative energy positions of the emission centers by fitting PL spectra with a sum of two Gaussians (Figure S21, Supporting Information). The higher energy band overlapped with the core's GSB and showed a ≈90 meV Stokes shift (Figure 3a), which was only twice larger than for the parental CdS/CdSe NRs, allowing us to assign this band to excitonic recombination. Even though the excitonic emission from ternary copper chalcogenides was rarely observed,[39–42,44,45] we can judge its presence from an almost linear dependence of the PL intensity on the excitation flux (PL intensity slope $I_{PL} = I_{ex}{}^{n}$ is tending to $n = 1$, see Figure S22a, Supporting Information) and significant narrowing of the emission line (full-width at half maximum was 110 meV, while for the most studied $CuInS_2$ nanocrystals, it is commonly in excess of 300 meV), which correlates well with the average $CuInS_2$ single-dot PL linewidth (128 meV).[68] Thus, we conclude that the narrow size distribution of the cation-exchange-derived CISe cores together with their efficient passivation by the CIS shell suppresses Cu-induced defects in the core and results in the excitonic recombination in our CISe/CIS NRs.

Contrastingly, the long-wavelength emission band has a PL intensity slope equal to $n \approx 0.7$ (Figure 4b, right panel), which is typical for defect-assisted recombination.[69] As mentioned earlier, the possible defect-assisted recombination pathway in ternary copper chalcogenides is the Cu^{1+}-related transition. The activation of the Cu^{1+} state requires photon absorption to form a photoinduced Cu^{2+} state, which should result in a long absorption tail that can be distinguished by an additional positive band in the TA spectra. However, we did not observe any additional TA bands at wavelengths longer than the core's GSB, while a band-like feature could be observed beyond the shell states in 780–820 nm range (Figure 3a). Unfortunately, this range coincides with the fundamental emission band of the Ti:Sapphire laser used for TA measurements, and thus cannot be clearly observed. However, the apparent Stokes shift (ΔS1, app), i.e., the shift between the VB-CB transition energy and the long-wavelength PL band maximum, is equal to 450 meV, which is in good agreement with Stokes shifts for Cu^{1+} emission reported previously.[68,70] Moreover, the location of Cu^{1+} defects in the shell can be inferred from the existence of the linear absorption tail (Figure S16, Supporting Information; Figure 3a). Considering significant surface damage for Cd-0 samples, which is more critical for the smaller core sizes as discussed above, a high amount of defects in the shell is to be expected. The PL decay time of this band largely depends on the Cd content and shortens from 385 ns (for 2.9 nm Cd-26 sample) to 285 nm (for 2.9 nm Cd-0 sample), which also supports its defect-related origin. The details on the PL decay times for all other samples are provided in Table S2 (Supporting Information).

From the results discussed above, we can summarize the following general trends in the emission of our CIS/CISe NRs. The excitonic band gradually blueshifts and its Stokes shift increases with increasing Cd content, while the maximum of the Cu^{1+}-related band depends weakly on Cd content (Table S1, Supporting Information). For the samples containing >20% of Cd, the

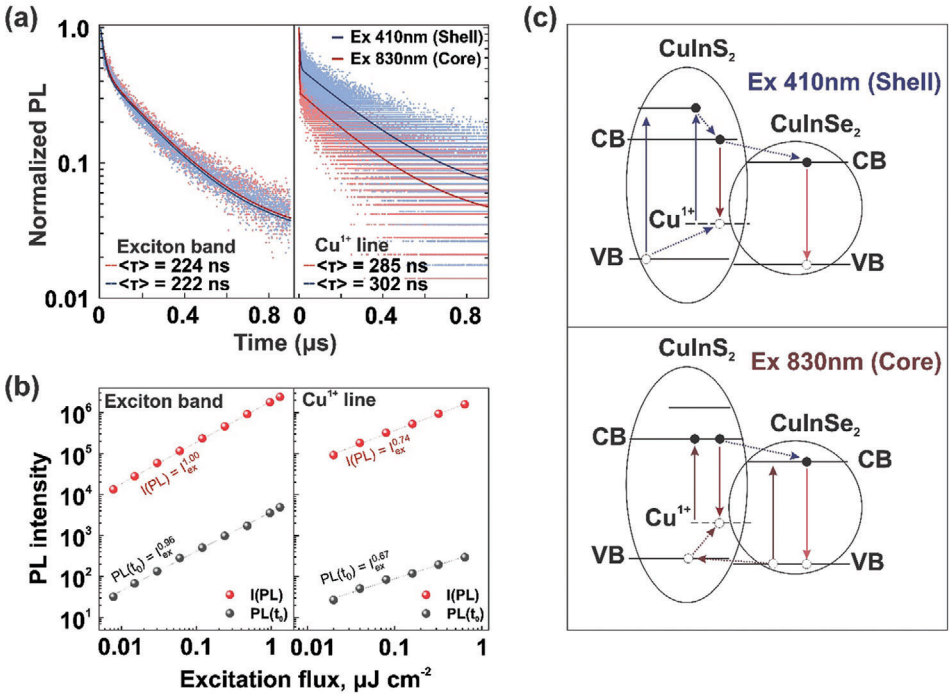

Figure 4. a) Time-integrated (I(PL)) and time-zero (PL(t_0)) PL intensities measured at 840 nm wherein the excitonic recombination dominates ("Exciton band" panel), and at 1000–1300 nm range corresponding to the primary emission from the Cu^{1+} band ("Cu^{1+} line" panel) of 2.9-nm Cd-0 NRs as a function of excitation flux. PL intensities were obtained from PL decay traces collected under resonant core excitation. b) PL decay traces of excitonic and Cu^{1+}-related bands under excitation of shell or core states. c) Schematic illustration of the main radiative recombination pathways (downward solid lines) and accompanying carriers transfers (dashed lines) for excitation above shell's bandgap (top panel) and resonant core excitation (bottom panel) in CISe/CIS NRs.

intensity of the Cu^{1+}-related PL band is higher than that of the excitonic one, indicating an increased amount of anti-site Cu_{In} – In_{Cu} pairs with a Cu^{1+} valency. As was mentioned in the Introduction, such defects are quite common for CIS nanocrystals with a stoichiometric Cu:In ratio. A lower Cu:In ratio (≈1:3.2, Figure 2a) in Cd-0 samples results in the domination of the excitonic recombination over the defect-assisted one and a narrowing of the excitonic emission line down to 110 meV, which, to the best of our knowledge, was never reported before for an ensemble of CuIn chalcogenide nanocrystals. The Cd content also affected the PL decay time of the CISe/CIS NRs, both for resonant core excitation (Figure S22 and Table S3, Supporting Information) and excitation above the shell's bandgap (Figure S24, Supporting Information). Both the average PL lifetime and the radiative recombination rate exhibited gradual change as the Cd content decreased (see Table S3 and Note S2, Supporting Information, for PL lifetime calculation details). Across all the samples with different Cd content (Cd-0, Cd-5, and Cd-26 samples) and for three different core sizes, the average PL lifetime shortened and the radiative recombination rate increased for decreasing Cd content, with an exception for the low Cd 2.7 nm core-sized NRs, which showed a significantly damaged surface during ligand exchange, as evidenced by the high non-radiative rate and broad PL peak.

Thus, the general picture of recombination pathways in CIS/CISe NRs can be described as follows (Figure 4c). Under excitation much above the shell bandgap (Figure 4c, upper panel), the simultaneous population of the shell's CB with electrons on Cu^{1+} defect activation occurs. Some of the photoexcited electrons from the shell's CB are transferred to the core's CB, while the remaining electrons recombine radiatively with Cu^{1+} defects. The efficiency of each of these processes is determined by the density of Cu^{1+} states in the CISe shell, which, in turn, depends on Cu:In stoichiometry and surface quality. Once electrons are transferred to the core's CB, they form excitons (not shown in Figure 4c), which then recombine radiatively.

Under resonant core excitation, direct oxidation of Cu^{1+} occurs with the electron transition to the shell's CB (Figure 4c, bottom panel). Similar to the shell excitation case, electrons from the shell's CB can either recombine with a copper defect or transfer to the core's CB. Ideally, resonant core excitation should result in more distinct excitonic PL, but we do not observe it due to hole transfer from core to shell. The hole transfer reduces the excitonic recombination probability in the core and favors the radiative recombination between CB's electrons and photoinduced Cu^{2+} defects. The efficiency of carrier transfer between the shell and the core (in both directions) is governed by Cd-induced interfacial defects, which again emphasizes the importance of Cd removal by means of the ligand displacement strategy proposed here. Comparison with other reports on ternary copper chalcogenide-based nano-emitters, given in **Table 1**, clearly shows that the proper surface passivation and Cd removal significantly enhance the light-emitting properties of cation exchanged CISe/CIS NRs, bringing their PL QY close to Zn-passivated counterparts.

Table 1. Summary of synthetic strategies used to fabricate core/shell $CuInSe_2/CuInS_2$ quantum dots (QD) or nanorods (NR) and related anisotropic ternary compounds, and their reported PL QY.

Material	Morphology/Crystal Structure	Synthesis method	PL QY, [%]	FWHM, [meV]	Report
CISe/CIS	NR/Wurtzite	Cation exchange	N/A	N/A	[8]
CISe/CIZS	"Giant shell" QD/Wurtzite	Cation exchange	1%	N/A	[6]
CISe/CIS (Cd<1 at.%)	NR/Wurtzite	Cation exchange	40%	172	This work[a)]
CISe/CIS (Cd~2–5 at.%)			18%	255	
CISe/CIS (Cd>20 at.%)			24%	268	
CISe/CIS	QD/Zinc blende	Hot injection	4.5%	310	[63]
CISe/CIZnSSe			20%	330	
CIS/ZnS	NR/Wurtzite	Hot injection	20%	308	[71]
CIZnS/CdS	NR/Wurtzite	Hot injection	45%	375	[49]

[a)] PL QY values listed here are provided for the 3.7 nm core NRs since they have the lowest degree of surface etching after cation exchange. PL QY values of all studied samples are listed in Table S2 (Supporting Information).

2.5. NIR FET Photodetectors Based on $CuInSe_2/CuInS_2$ NRs

To investigate the influence of intrinsic defects and the synthetic route on the device-related characteristics of the obtained CISe/CIS NRs, we have fabricated photodetectors with a bottom gate FET configuration (**Figure** 5a) from NRs with different cadmium content discussed above, i.e., Cd-0 (<1 at.%), Cd-5 (2–5 at.%), and Cd-26 NRs (14–26 at.%). 2.9 nm CISe/CIS NRs were employed as an active layer in the FET device, as they serve as a model system to study the effects of etching and low cadmium content, while still preserving the NR shape.

To achievehigh figures-of-merits of FETs, the original long-chain ligands on CISe/CIS NRs were replaced by shorter ligand $(NH_4)_2S$ during the liquid phase ligand exchange. Initially, the transport properties of the CISe/CIS NRs nanorods in FETs were examined in the dark at a variable bias (Figure 5b; Figure S25, Supporting Information). We recall that the NRs were confirmed to be copper-deficient by ICP-AES, and indeed these Cu vacancies ensured the p-type conductivity of their films (Figure S25, Supporting Information). Notably, the I-V characteristics were significantly influenced by the Cd content in the studied NRs. It was observed that the removal of Cd impurities could reduce undesired hysteresis and enhance the photocurrent (Figure 5c). Furthermore, the two-step ligand exchange process led to the passivation of the surface defects, mitigating its effect on the number of carriers available for photoconduction and favoring slightly higher current modulation for Cd-free detectors (Figure S25d–f, Supporting Information). The highest carrier mobility among the studied structures was achieved for the Cd-0 sample and equals to 5×10^{-4} cm^2 V^{-1} s^{-1} under 685 nm laser light at 300 K (Figure S26, Supporting Information). It was also observed that the device performance was strongly affected by temperature (Figure S26, Supporting Information), highlighting the dominant role of the defect-related charge carrier transport in the NR films. Higher charge carrier hopping activation energies for cadmium-containing samples (Figure S26, Supporting Information) can be attributed to a larger number of traps in Cd-5 and Cd-26 samples.

All the 3 kinds of FET samples (based on Cd-0, Cd-5, and Cd-26 NRs) exhibited nonlinear dependence of the photocurrent and responsivity on the illumination intensity increase (Figure 5c; Figure S27, Supporting Information). The excitation power dependence of the photocurrent ($I_{pc} \approx P_{in}{}^{\alpha}$, where α = 0.5) indicates the influence of the higher-order recombination process[72,73] due to a low Auger threshold. On the other hand, the noise current density of the Cd-0 sample was two orders of magnitude lower than that of the Cd-26 sample (Figure 5d). This difference ensures a specific detectivity D^* up to 10^8 Jones at 685 nm of the Cd-0-based device, as derived using the equation $D^* = \frac{R\sqrt{A}}{i_n}$, where R is responsivity (A W^{-1}), A is the device area (cm^2), and i_n is the noise current density (A $Hz^{-1/2}$), (Figure 5e). It should be noted that the specific detectivity of most of the devices reported in the literature and listed in Table S4 (Supporting Information) was calculated using the formula $D^* = \frac{R}{\sqrt{2qJ_d}}$, where R represents the responsivity (A W^{-1}), q is the elementary charge (C), and J_d is the dark current density (A cm^{-2}). However, this formula only takes into account the shot noise of the photodetector. As a result, the values obtained for the specific detectivity using the latter equation are consistently overestimated compared to calculations that consider the "full" noise current density, which consists of Johnson, shot, flicker, and burst noise.[74] For instance, for our system, the specific detectivity value would be as high as 2×10^{11} Jones if using the previous approximate formula, contrasting with the 10^8 Jones that we report using the actual *measured* noise. The correct noise current in the expression, $D^* = \frac{R\sqrt{A}}{i_n}$, should be the square root of the sum of all the squares of each noise current contribution.[75] Often it is assumed that a $1/\sqrt{frequency}$ dependence for the noise current (often seen) indicates that flicker noise is by far dominant (at least over some low frequency range). However, our data for the present materials in Figure 4d is a clear illustration of where an assumed single noise contribution is not a good assumption, and where actual measured noise current data are necessary. Figure 4d shows the flicker noise is peeled away to

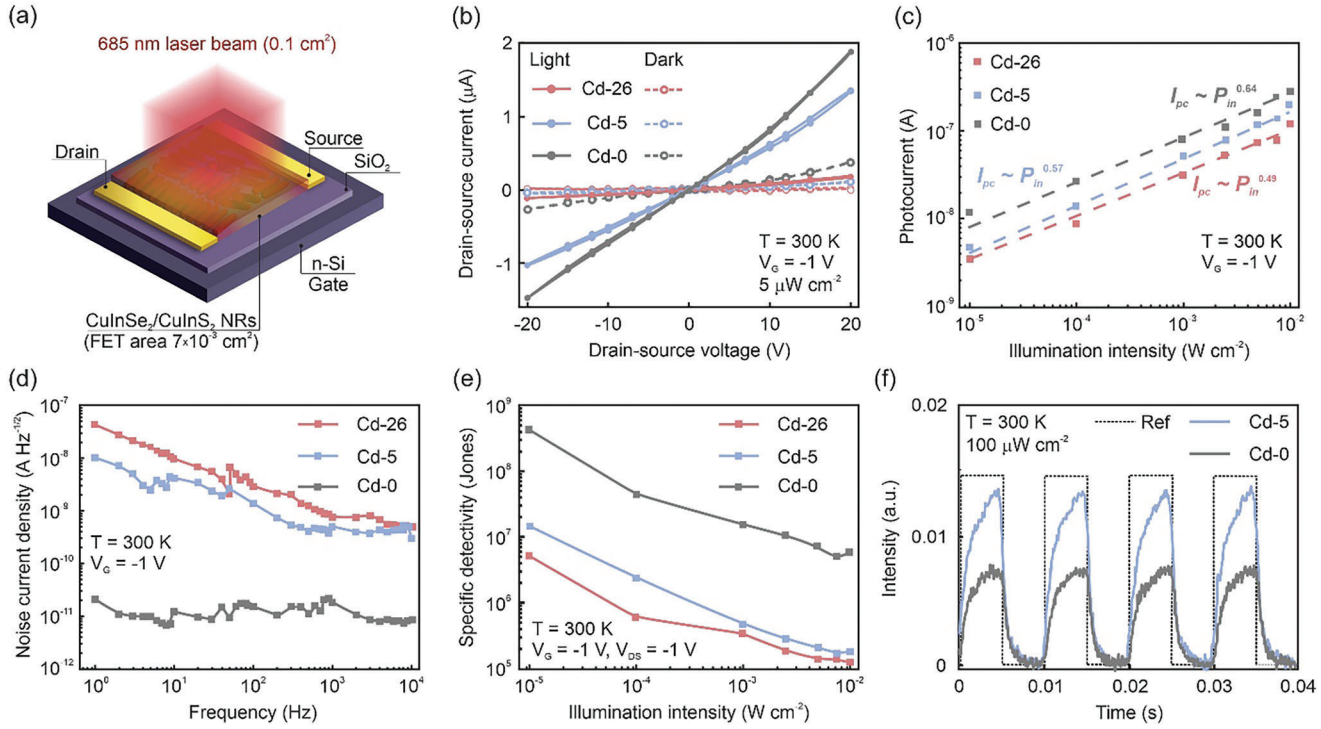

Figure 5. a) A sketch of FET based on CISe/CIS NRs; the channel width and length are 0.001 and 0.065 cm, respectively; b) Output I_{DS}–V_{DS} curves for the NR samples with different Cd content (Cd-0, Cd-5, and Cd-26; see text); c) Photocurrent I_{pc} dependence for the 3 kinds of NR samples on the illumination intensity P_{in}; d) Noise current density of the FETs based on 3 kinds of NR samples measured in the dark at room temperature; e) Specific detectivity of the FETs based on 3 kinds of NR samples under 685 nm laser illumination and low bias of −1 V; f) Response time of the devices based on Cd-0 and Cd-5 NRs under pulsed laser illumination.

a large degree through improved cation purity after treatment, giving rise to an almost "*white*" noise spectrum when almost all residual Cd is removed. We believe it is crucial to consider all factors that contribute to the obscuring of the photodetector signal. Therefore, although the calculated specific detectivity value is lower than reported in some other studies, we prefer to use more reliable estimations as presented in this work. Moreover, the presented photodetectors here were fabricated without annealing, thus featuring non-sintered NC-based devices.

Both the responsivity and the specific detectivity of all samples decreased significantly with increasing illumination intensity for all devices regardless of cadmium content. By adjusting the gate bias, it was possible to enhance the response efficiency in the linear regime under low V_{DS} conditions (Figure S28, Supporting Information). In turn, the influence of Cd content on the photodetector's time-resolved response was found to be significant (Figure 5f). Due to the high noise current density of the Cd-26 sample, it was not possible to register a time-resolved response signal, even with the application of filters on the signal pre-amplifier. In contrast, the rise time of both Cd-5 and Cd-0 devices was estimated as 3.5 ms, while the fall time was found to drop from 2.1 to 1.9 ms after the complete removal of Cd (Figure 5f).

Overall, as summarized in Table S4 (Supporting Information), the figures-of-merit of the photodetectors with our CISe/CIS NRs as the active material are among the highest reported for $CuInX_2$ (where X = S, Se) nanocrystal-based devices. Although the hole mobility of CISe/CIS NRs is still lower than that of the bulk-like material (Table S4, Supporting Information) or commercially available InAs and Si photodetectors,[75] the values of responsivity and specific detectivity are comparable to those achieved by combining several types of QDs and heterostructures in other photodetector systems.[22,23,76] Still, there exist challenges related to synthesis scalability, material uniformity, and long-term stability which are slowing down the development and commercialization of nanocrystal-based photodetectors. Taking into account market-successful counterparts such as CMOS, CCD, or, for example, InGaAs NIR photodiodes, careful material and device engineering is required to bring the CIS-family photodetectors to a competitive level. Our results highlight the promising potential of CISe/CIS NRs as an environmentally benign material for optoelectronic applications.

3. Conclusion

Ligands play several important roles in cation exchange reactions, balancing the cation inflow and outflow and improving the colloidal stability of nanocrystals on one hand, while on the other hand eventually contaminating the final products with unwanted cations from the host material. The latter issue is important if the final goal is to produce heavy-metal-free nanocrystals from Cd- or Hg-based ones. We have shown that Cd-phosphonates bound to CdSe/CdS NRs remain at the surface of $Cu_{2-x}Se/Cu_{2-x}S$ NRs derived thereof, leading to rather high (2–5 at.%) residual

Cd content in the final $CuInSe_2/CuInS_2$ NRs. Alkylamine-driven ligand exchange allowed us to remove most of the Z-type Cd-phosphonates from the surface of $Cu_{2-x}Se/Cu_{2-x}S$ NRs, but this somewhat compromised their colloidal stability. We thus introduced a two-step ligand exchange strategy, where at the first step octylamine was combined with TOPO to avoid aggregation of the $Cu_{2-x}Se/Cu_{2-x}S$ NRs after Cd-phosphonate replacement. In the second step, the Z-type ligand component of the $Cu_{2-x}Se/Cu_{2-x}S$ NRs was replenished by the addition of In-phosphonates in order to passivate anionic surface sites. This procedure enabled us to obtain CISe/CIS NRs with very low residual Cd content (<1 at.%), which was accompanied by some reduction in the diameter/length of the rods due to the surface etching by the octylamine-TOPO mixture. The obtained CISe/CIS NRs had the highest PL QY (40%) ever reported for heavy-metal-free NIR emitting CuIn chalcogenide nanocrystals (Table 1), which certifies wide prospects of the suggested method toward producing high-quality colloidal nanoheterostructures via cation exchange. TA studies revealed that electron localization occurs within the CISe core, while holes are distributed throughout both core and shell states, suggesting a quasi-type II heterostructure for CISe/CIS NRs. Furthermore, the deconvolution of the PL spectra into contributions from different recombination channels revealed the appearance of a rather narrow (≈110 meV) excitonic emission line which was not seen in copper-indium chalcogenides produced by direct synthesis. Meanwhile, the increase of the Cd content via the ligand displacement procedure broadened the excitonic emission line up to 180 meV. Improvements and understanding of the cation exchange procedure gained in this study open up vast prospects for future applications for nanomaterial synthesis.

Moreover, the developed two-step cation exchange and ligand replacement procedure offered favorable outcomes not only for the high PL QY but also for the electrical properties of CISe/CIS NRs in their films. FET-photodetectors based on unannealed CISe/CIS NRs demonstrated high responsivity of up to 0.2 A W^{-1} and specific detectivity of 10^8 Jones at 685 nm. Overall, the device performance of the CISe/CIS NRs ranks among the highest reported for nanocrystal-based optoelectronics. Continued research and optimization efforts in synthesis and device engineering based on such NIR CISe/CIS NRs hold high potential to further enhance their performance and expand their applications in optoelectronic devices.

Supporting Information

Supporting Information is available from the Wiley Online Library or from the author.

Acknowledgements

The authors acknowledge financial support from the Research Grants Council of Hong Kong SAR (SRFS2324-1S04 and C7035-20G), Innovation and Technology Fund of Hong Kong SAR (ITS/027/22MX), Technology and Innovation Commission of Shenzhen Municipality (HZQB-KCZYB-2020031), and Science and Technology Department of Sichuan Province (2021YFSY0016). This work made use of resources from the TRACE TEM center at the City University of Hong Kong.

Conflict of Interest

The authors declare no conflict of interest.

Author Contributions

A.P., A.S., and K.S. contributed equally to this work. A.P. conceived the idea, designed the experiments, and conducted materials synthesis and characterization. A.S. performed optical spectroscopy studies. K.S. fabricated photodetectors and conducted device testing. C.C.S.C. and K.S.W. contributed to optical spectroscopy analysis and results discussion. Z.L. and X.Z. analyzed TEM data. S.W., J.N., and S.V.K. assisted with manuscript preparation. A. R. directed the research project. A.P., A.S., K.S., and A.R. wrote the manuscript. All authors discussed and analyzed the results.

Data Availability Statement

The data that support the findings of this study are available in the supplementary material of this article.

Keywords

cation exchange, infrared photodetectors, ligand exchange, near-infrared emission, ternary chalcogenide nanorods

Received: January 16, 2024
Revised: March 3, 2024
Published online: March 13, 2024

[1] S. Gupta, S. V. Kershaw, A. L. Rogach, *Adv. Mater.* **2013**, *25*, 6923.
[2] D. H. Son, S. M. Hughes, Y. Yin, A. Paul Alivisatos, *Science* **2004**, *306*, 1009.
[3] L. De Trizio, L. Manna, *Chem. Rev.* **2016**, *116*, 10852.
[4] J. B. Rivest, P. K. Jain, *Chem. Soc. Rev.* **2013**, *42*, 89.
[5] E. Izquierdo, A. Robin, S. Keuleyan, N. Lequeux, E. Lhuillier, S. Ithurria, *J. Am. Chem. Soc.* **2016**, *138*, 10496.
[6] X. Tong, X.-T. Kong, Y. Zhou, F. Navarro-Pardo, G. S. Selopal, S. Sun, A. O. Govorov, H. Zhao, Z. M. Wang, F. Rosei, *Adv. Energy Mater.* **2018**, *8*, 1701432.
[7] H. Li, R. Brescia, R. Krahne, G. Bertoni, M. J. P. Alcocer, C. D'Andrea, F. Scotognella, F. Tassone, M. Zanella, M. De Giorgi, L. Manna, *ACS Nano* **2012**, *6*, 1637.
[8] W. van der Stam, E. Bladt, F. T. Rabouw, S. Bals, C. de Mello Donega, *ACS Nano* **2015**, *9*, 11430.
[9] D. Li, S. Huang, X. Zhang, Z. Nazir, Y. Li, J. Zhang, Y. Chen, H. Zhong, *J. Phys. Chem. Lett.* **2020**, *11*, 7.
[10] C. Dabard, J. Planelles, H. Po, E. Izquierdo, L. Makke, C. Gréboval, N. Moghaddam, A. Khalili, T. H. Dang, A. Chu, S. Pierini, C. Abadie, M. Cavallo, E. Bossavit, X. Z. Xu, P. Hollander, M. Silly, E. Lhuillier, J. I. Climente, S. Ithurria, *Chem. Mater.* **2021**, *33*, 9252.
[11] R. Tu, Y. Xie, G. Bertoni, A. Lak, R. Gaspari, A. Rapallo, A. Cavalli, L. De Trizio, L. Manna, *J. Am. Chem. Soc.* **2016**, *138*, 7082.
[12] P. K. Jain, L. Amirav, S. Aloni, A. P. Alivisatos, *J. Am. Chem. Soc.* **2010**, *132*, 9997.
[13] D. Lee, W. D. Kim, S. Lee, W. K. Bae, S. Lee, D. C. Lee, *Chem. Mater.* **2015**, *27*, 5295.
[14] I. Kriegel, A. Wisnet, A. R. Srimath Kandada, F. Scotognella, F. Tassone, C. Scheu, H. Zhang, A. O. Govorov, J. Rodríguez-Fernández, J. Feldmann, *J. Mater. Chem. C* **2014**, *2*, 3189.
[15] K. Miszta, G. Gariano, R. Brescia, S. Marras, F. De Donato, S. Ghosh, L. De Trizio, L. Manna, *J. Am. Chem. Soc.* **2015**, *137*, 12195.

[16] F. Li, M. Zhang, D. Benetti, L. Shi, L. V. Besteiro, H. Zhang, J. Liu, G. S. Selopal, S. Sun, Z. Wang, Q. Wei, F. Rosei, *Appl. Catal. B Environ.* **2021**, *280*, 119402.
[17] X. Yang, F. Ren, Y. Wang, T. Ding, H. Sun, D. Ma, X. W. Sun, *Sci. Rep.* **2017**, *7*, 14741.
[18] G. J. Supran, K. W. Song, G. W. Hwang, R. E. Correa, J. Scherer, E. A. Dauler, Y. Shirasaki, M. G. Bawendi, V. Bulović, *Adv. Mater.* **2015**, *27*, 1437.
[19] F. Huang, J. Ning, Z. Duan, A. A. Sergeev, A. Portniagin, S. V. Kershaw, J. Tian, A. L. Rogach, *Chem. Mater.* **2021**, *33*, 2398.
[20] X. Bai, F. Purcell-Milton, Y. Gun'ko, *Nanomaterials* **2019**, *9*, 85.
[21] H. Liu, M. Yu, F. Qin, W. Feng, P. Hu, *ACS Appl. Nano Mater.* **2018**, *1*, 5414.
[22] T. Shen, F. Li, Z. Zhang, L. Xu, J. Qi, *ACS Appl. Mater. Interfaces* **2020**, *12*, 54927.
[23] R. Guo, F. Huang, K. Zheng, T. Pullerits, J. Tian, *ACS Appl. Mater. Interfaces* **2018**, *10*, 35656.
[24] H. J. Yun, J. Lim, J. Roh, D. C. J. Neo, M. Law, V. I. Klimov, *Nat. Commun.* **2020**, *11*, 5280.
[25] C. Pang, S. Hu, C. Guo, J. Wang, S. Zou, Z. Pan, J. Liu, L. Shen, N. Bao, H. Ning, A. Gupta, Z. Gong, *Chem. Mater.* **2021**, *33*, 8775.
[26] V. Bhatt, M. Kumar, E. C. Kim, H. J. Chung, J. H. Yun, *ACS Appl. Electron. Mater.* **2022**, *4*, 6284.
[27] Z. Zheng, J. Yao, G. Yang, *ACS Appl. Mater. Interfaces* **2017**, *9*, 7288.
[28] M. Li, J. Xu, K. Zhu, S. Shi, Q. Zhang, Y. Bu, J. Chen, J. Xu, Q. Zheng, Y. Su, X. Zhang, L. Li, *J. Mater. Chem. C* **2021**, *9*, 14613.
[29] A. Prudnikau, H. Roshan, F. Paulus, B. Martín-García, R. Hübner, H. Bahmani Jalali, M. De Franco, M. Prato, F. Di Stasio, V. Lesnyak, *Adv. Funct. Mater.* **2023**, *1*, 2310067.
[30] C. Xia, J. D. Meeldijk, H. C. Gerritsen, C. De Mello Donega, *Chem. Mater.* **2017**, *29*, 4940.
[31] W. van der Stam, A. C. Berends, F. T. Rabouw, T. Willhammar, X. Ke, J. D. Meeldijk, S. Bals, C. de Mello Donega, *Chem. Mater.* **2015**, *27*, 621.
[32] L. Makké, N. Fu, H. Lehouelleur, H. Po, C. Dabard, L. Curti, E. Bossavit, X. Z. Xu, G. Patriarche, D. Pierucci, M. G. Silly, E. Lhuillier, S. Ithurria, *Chem. Mater.* **2023**, *35*, 9581.
[33] M. A. Boles, D. Ling, T. Hyeon, D. V. Talapin, *Nat. Mater.* **2016**, *15*, 141.
[34] I. Moreels, B. Fritzinger, J. C. Martins, Z. Hens, *J. Am. Chem. Soc.* **2008**, *130*, 15081.
[35] N. C. Anderson, M. P. Hendricks, J. J. Choi, J. S. Owen, *J. Am. Chem. Soc.* **2013**, *135*, 18536.
[36] J. M. Luther, H. Zheng, B. Sadtler, A. P. Alivisatos, *J. Am. Chem. Soc.* **2009**, *131*, 16851.
[37] A. S. Portniagin, K. A. Sergeeva, S. V. Kershaw, A. L. Rogach, *Chem. Mater.* **2023**, *35*, 5631.
[38] J. C. Flanagan, L. P. Keating, M. N. Kalasad, M. Shim, *Chem. Mater.* **2019**, *31*, 9307.
[39] A. Fuhr, H. J. Yun, S. A. Crooker, V. I. Klimov, *ACS Nano* **2020**, *14*, 2212.
[40] D. H. Jara, K. G. Stamplecoskie, P. V. Kamat, *J. Phys. Chem. Lett.* **2016**, *7*, 1452.
[41] J. Chen, L. Zhang, S. Li, F.-L. Jiang, P. Jiang, Y. Liu, *ACS Appl. Nano Mater.* **2021**, *4*, 6057.
[42] W. van der Stam, M. de Graaf, S. Gudjonsdottir, J. J. Geuchies, J. J. Dijkema, N. Kirkwood, W. H. Evers, A. Longo, A. J. Houtepen, *ACS Nano* **2018**, *12*, 11244.
[43] A. Harchol, Y. Barak, K. E. Hughes, K. H. Hartstein, H. J. Jöbsis, P. T. Prins, C. De Mello Donegá, D. R. Gamelin, E. Lifshitz, *ACS Nano* **2022**, *16*, 12866.
[44] A. S. Fuhr, H. J. Yun, N. S. Makarov, H. Li, H. McDaniel, V. I. Klimov, *ACS Photonics* **2017**, *4*, 2425.
[45] W. D. Rice, H. McDaniel, V. I. Klimov, S. A. Crooker, *J. Phys. Chem. Lett.* **2014**, *5*, 4105.
[46] L. Carbone, C. Nobile, M. De Giorgi, F. D. Sala, G. Morello, P. Pompa, M. Hytch, E. Snoeck, A. Fiore, I. R. Franchini, M. Nadasan, A. F. Silvestre, L. Chiodo, S. Kudera, R. Cingolani, R. Krahne, L. Manna, *Nano Lett.* **2007**, *7*, 2942.
[47] D. V. Talapin, J. H. Nelson, E. V. Shevchenko, S. Aloni, B. Sadtler, A. P. Alivisatos, *Nano Lett.* **2007**, *7*, 2951.
[48] M. Jiao, A. S. Portniagin, X. Luo, L. Jing, B. Han, A. L. Rogach, *Adv. Opt. Mater.* **2022**, *10*, 2200226.
[49] A. S. Portniagin, J. Ning, S. Wang, Z. Li, A. A. Sergeev, S. V. Kershaw, X. Zhong, A. L. Rogach, *Adv. Opt. Mater.* **2022**, *10*, 2102590.
[50] H. Lei, J. Li, X. Kong, L. Wang, X. Peng, *Acc. Chem. Res.* **2023**, *56*, 1966.
[51] E. Weiss, *Acc. Chem. Res.* **2013**, *46*, 2607.
[52] R. Luschtinetz, G. Seifert, E. Jaehne, H.-J. P. Adler, *Macromol. Symp.* **2007**, *254*, 248.
[53] B. Zeng, G. Palui, C. Zhang, N. Zhan, W. Wang, X. Ji, B. Chen, H. Mattoussi, *Chem. Mater.* **2018**, *30*, 225.
[54] P. E. Chen, N. C. Anderson, Z. M. Norman, J. S. Owen, *J. Am. Chem. Soc.* **2017**, *139*, 3227.
[55] C. Xia, A. Pedrazo-Tardajos, D. Wang, J. D. Meeldijk, H. C. Gerritsen, S. Bals, C. de Mello Donega, *Chem. Mater.* **2021**, *33*, 102.
[56] Y. Wang, Y. Hu, Q. Zhang, J. Ge, Z. Lu, Y. Hou, Y. Yin, *Inorg. Chem.* **2010**, *49*, 6601.
[57] S. C. Riha, D. C. Johnson, A. L. Prieto, *J. Am. Chem. Soc.* **2011**, *133*, 1383.
[58] H. Li, R. Brescia, M. Povia, M. Prato, G. Bertoni, L. Manna, I. Moreels, *J. Am. Chem. Soc.* **2013**, *135*, 12270.
[59] A. Antanovich, A. Prudnikau, A. Matsukovich, A. Achtstein, M. Artemyev, *J. Phys. Chem. C* **2016**, *120*, 5764.
[60] N. Kirkwood, J. O. V. Monchen, R. W. Crisp, G. Grimaldi, H. A. C. Bergstein, I. du Fossé, W. van der Stam, I. Infante, A. J. Houtepen, *J. Am. Chem. Soc.* **2018**, *140*, 15712.
[61] J. L. Stein, E. A. Mader, B. M. Cossairt, *J. Phys. Chem. Lett.* **2016**, *7*, 1315.
[62] C. H. M. van Oversteeg, F. E. Oropeza, J. P. Hofmann, E. J. M. Hensen, P. E. de Jongh, C. de Mello Donega, *Chem. Mater.* **2019**, *31*, 541.
[63] J. Ning, Y. Xiong, F. Huang, Z. Duan, S. V. Kershaw, A. L. Rogach, *Chem. Mater.* **2020**, *32*, 7842.
[64] L. De Trizio, M. Prato, A. Genovese, A. Casu, M. Povia, R. Simonutti, M. J. P. Alcocer, C. D'Andrea, F. Tassone, L. Manna, *Chem. Mater.* **2012**, *24*, 2400.
[65] L. Li, A. Pandey, D. J. Werder, B. P. Khanal, J. M. Pietryga, V. I. Klimov, *J. Am. Chem. Soc.* **2011**, *133*, 1176.
[66] C. C. S. Chan, K. Fan, H. Wang, Z. Huang, D. Novko, K. Yan, J. Xu, W. C. H. Choy, I. Lončarić, K. S. Wong, *Adv. Energy Mater.* **2021**, *11*, 2003071.
[67] G. Grimaldi, J. J. Geuchies, W. van der Stam, I. du Fossé, B. Brynjarsson, N. Kirkwood, S. Kinge, L. D. A. Siebbeles, A. J. Houtepen, *Nano Lett.* **2019**, *19*, 3002.
[68] H. Zang, H. Li, N. S. Makarov, K. A. Velizhanin, K. Wu, Y.-S. Park, V. I. Klimov, *Nano Lett.* **2017**, *17*, 1787.
[69] S. Tongay, J. Suh, C. Ataca, W. Fan, A. Luce, J. S. Kang, J. Liu, C. Ko, R. Raghunathanan, J. Zhou, F. Ogletree, J. Li, J. C. Grossman, J. Wu, *Sci. Rep.* **2013**, *3*, 2657.
[70] M. Sandroni, K. D. Wegner, D. Aldakov, P. Reiss, *ACS Energy Lett.* **2017**, *2*, 1076.
[71] C. Xia, N. Winckelmans, P. T. Prins, S. Bals, H. C. Gerritsen, C. de Mello Donegá, *J. Am. Chem. Soc.* **2018**, *140*, 5755.
[72] D. Kufer, I. Nikitskiy, T. Lasanta, G. Navickaite, F. H. L. Koppens, G. Konstantatos, *Adv. Mater.* **2015**, *27*, 176.
[73] M. Chen, H. Lu, N. M. Abdelazim, Y. Zhu, Z. Wang, W. Ren, S. V. Kershaw, A. L. Rogach, N. Zhao, *ACS Nano* **2017**, *11*, 5614.
[74] P. Horowitz, W. Hill, in *The Art of Electronics*, Cambridge University Press, New York, NY **2015**.
[75] A. Rogalski, *ACS Photonics* **2023**, *10*, 647.
[76] R. Guo, C. Bao, F. Gao, J. Tian, *Adv. Opt. Mater.* **2020**, *8*, 1.